Robotica (2019) volume 37, pp. 521–538. © Cambridge University Press 2018
doi:10.1017/S0263574718001157

Design of a miniature modular inchworm robot with an anisotropic friction skin

Wael Saab, Peter Racioppo, Anil Kumar and Pinhas Ben-Tzvi*

Robotics and Mechatronics Laboratory, Mechanical Engineering, Electrical and Computer Engineering, Virginia Tech, Blacksburg, VA 24061, USA. E-mails: waelsaab@vt.edu, rpeter8@vt.edu, anilks@vt.edu

(Accepted 08, 2018 August. First published online: October 30, 2018)

SUMMARY

This paper presents the design, analysis, and experimental validation of a miniature modular inchworm robot (MMIR). Inchworm robots are capable of maneuvering in confined spaces due to their small size, a desirable characteristic for surveillance, exploration and search and rescue operations. This paper presents two generations of the MMIR (Version 1—V1 and Version 2—V2) that utilize anisotropic friction skin and an undulatory rectilinear gait to produce locomotion. This paper highlights design improvements and a multi-body dynamics approach to model and simulate the system. The MMIR V2 incorporates a slider-crank four-bar mechanism and a relative body revolute joint to produce high-frequency relative translation and rotation to increase forward velocity and enable turning capabilities. Friction analysis and locomotion experiments were conducted to assess the systems performance on various surfaces, validate the dynamic model and simulation results, and measure the maximum forward velocity. The MMIR V1 and V2 were able to achieve maximum forward velocities of 12.7 mm/s and 137.9 mm/s, respectively. These results are compared to reported results of similar robots published in the literature.

KEYWORDS: Design, Mobile robots, Robot dynamics, Mechatronics systems

1. Introduction

Animals have evolved over millions of years to adapt to their natural habitat. They utilize a wide variety of skin types and locomotion mechanisms to traverse terrain, ranging from legged locomotion using limbs, to inchworm-like locomotion that involves repeated body expansions and contractions. For example, geckos can climb up inclined surfaces using directional foot pads that have millions of microscopic hair-like bristles called setae that provide directional adhesion properties.[1] Gastropods adhere to a surface using a thin layer of mucus covering their skin and generate rhythmic muscular wave undulations to create differences in reactive and frictional forces, which result in forward locomotion.[2] It has also been observed that the leaf beetle's forward pulling force increases with the numbers of slanted setae on its legs, and can prevent the animal from slipping backward.[3] These animals have inspired engineers to develop bio-inspired robots that utilize similar locomotion mechanisms and skin properties found in nature.[4–6]

Legged robots have been developed in the literature. However, they require a large number of actuators and potentially complicated body structures to mimic the locomotion patterns of their animal counterparts.[7–9] Since it is difficult to apply such mechanisms for small-scale applications, snake and inchworm-like robotic structures have been investigated for meso-scale robotic applications.[10–12]

The majority of published snake and inchworm robots utilize vertical wave undulation to produce locomotion.[13,14] This involves lifting body parts above the ground and displacing them forward

* Corresponding author. E-mail: bentzvi@vt.edu

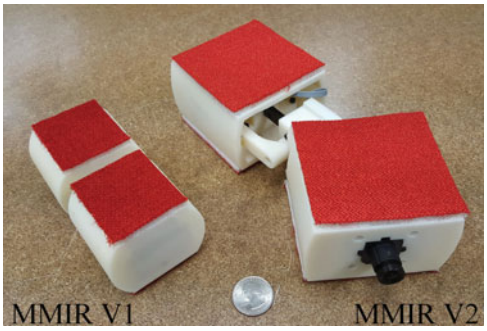

Fig. 1. Side by side view of the: (Left) first and (Right) second generation modular inch worm robot.

with respect to the remaining stationary body. This type of locomotion is appealing for robotic applications since the additional space and costs of treads or wheels is not required. This gait also enables locomotion on a wide variety of terrains, as the robot can adjust its shape to fit the terrain contour. However, because of the wasted time and energy spent on lifting and lowering the modules normal to the robot's trajectory, this motion can result in low forward velocities with limited operation time. Additionally, the extra required energy necessitates a larger chassis for storing additional sources of energy and makes these robots less suitable for operation in confined spaces.[15]

To address these issues, we propose an inchworm robot that utilizes anisotropic friction characteristics and produces high speed, undulatory rectilinear motion through relative linear expansion and contraction between two bodies, without the need to lift body parts above the ground. Although variations of this concept have been proposed in the literature, the majority of these robots utilize custom designed components that require high manufacturing costs, as discussed in Section 2.1.

This paper presents the design evolution of the Miniature Modular Inchworm Robot (MMIR), shown in Fig. 1. The authors extend preliminary research[16] and present the analysis of a second generation design concept that utilizes an anisotropic friction skin (AFS), and a slider-crank four-bar mechanism and a relative-rotation servomotor to produce high-speed forward locomotion and turning, respectively. A multi-body dynamics approach is used to model and simulate the system's equations of motion, which are verified experimentally with integrated prototypes. This paper also presents an in-depth analysis of the AFS properties and comparative analysis of the proposed robot's performance with similar robots published in the literature. The aim of this research is to develop small-scale, low-cost robots that are capable of mapping indoor environments and to investigate their performance in producing locomotion on various types of surfaces through modeling, simulation, and experimentation. Such a small-scale robot that utilizes anisotropic friction as a means to produce locomotion provides the advantages of mechanical design redundancy and miniaturization, and minimized control efforts.[17]

The structure of this paper is as follows. Section 2 presents a literature review pertaining to robot designs which utilize adhesion or anisotropic friction characteristics to produce locomotion and to locomotion modeling of these robotic systems. Section 3 reviews the MMIR V1 design. Section 4 presents the MMIR V2 and highlights design improvements. Section 5 presents the locomotion strategy to achieve forward locomotion and steering capabilities. Section 6 presents dynamic modeling of the robotic system using a multi-body dynamics approach with generalized coordinates. Section 7 presents experimental results of friction analysis and the assessment of locomotion capabilities of the proposed robots compared to both simulation results of the dynamic model and to the performance of robots published in literature. Concluding remarks and future work are discussed in Section 8.

2. Related Work

This section reviews the state of the art of robot designs that utilize adhesion or friction properties to produce locomotion, and of locomotion modeling of these robotic systems.

2.1. Robot designs

The slim slime robot[18] was designed with three serially connected modules actuated by bellows that are capable of shrinking, stretching, and locking, enabling three-dimensional locomotion. The robot demonstrated a maximum forward velocity of 60 mm/s (8.21e–2 body lengths per second) by sliding only one module forward at a time, while the combined friction forces of the remaining two stationary modules, prevented backward slippage. The robot measured 128 mm in diameter, with a total contracted length of 730 mm.

Similarly, the Active Cord Mechanism—R5 robot[19] was designed with a three-degree of freedom (DOF) bending and expanding joint unit with six ratchet wheels surrounding each body segment. This configuration enabled both inchworm and angleworm-type motions. The robot measured 80 mm in diameter and 1600 mm in length. Inchworm-type motion demonstrated a slow gait, but was capable of traversing bumpy or uneven ground. In contrast, the angleworm-type motion used little energy for fast motion on flat ground up to 400 mm/s (0.25 body lengths per second), but demonstrated less efficient locomotion on uneven ground. Similarly, Ma *et al.* developed a snake-like robot[20] composed of four modules, with passive unidirectional wheels surrounding its outer circumference, each capable of yaw, roll, and sliding motion that enabled both serpentine and rectilinear locomotion. The robot measured 120 mm in diameter and 680 mm in length and demonstrated a maximum velocity of 8 mm/s (1.17e–2 body lengths per second). The unidirectional wheels provided more efficient locomotion due to anisotropic friction characteristics, in comparison to a previous design that utilized conventional wheels.[21]

The Maryland Snake Inspired Robot[15] consisted of three-DOF joint modules, each with two revolute joints, which rotated in orthogonal planes with respect to one another, and a prismatic joint. Joint modules were stacked serially, with 90° roll offsets, and a one-DOF friction-anchor module was placed at either end of the robot to grip the environment. To achieve either turning or forward motion, the joint modules would perform either rotation or linear expansion, respectively, and alternate between high and low friction forces using the anchor during a gait cycle. The robot had a compressed length of 1003 mm and extended length of 1384 mm, with a cross-section of 70 × 70 mm and could move forward at a speed of 167 mm/s (0.167 body lengths per s).

Chen *et al.* proposed a planar inchworm robot[22] designed for applications in narrow and confined spaces, such as pipes and conduits. The robot consisted of one-DOF modules that could function as either grippers, to enhance adhesion to the surface, or extensors that could deform in the direction of the robot's motion. Further research into this design concept resulted in the development of the planar walker.[23] It contained linear cylinders and four revolute joints to form a closed-loop, eight-bar mechanism. Four pneumatic suction modules were mounted below each revolute joint, to adhere to a terrain surface. While it mimicked snake or inchworm-like creeping motions, its mechanical design also enabled swift changes in the direction of travel. The robot measured 710 mm in length and could produce a forward velocity of 1 mm/s (1.41e–3 body lengths per s).

An earthworm-like robot[10] utilized a shape memory alloy actuator between two segments to create relative translation between the two bodies. Each body had a passive needle that could grip onto a soft environment to prevent backward slipping. The robot measured 50 mm in length and 9.5 mm in diameter, and could produce a forward velocity of 0.16 mm/s (3.20e–3 body lengths per s).

An earthworm robot was presented in ref. [24] that consisted of eight, soft body segments, capable of expansion and contraction by pulling cables. The robot generated forward locomotion by keeping the majority of its body segments stationary while sliding the remaining segments forward. This gait procedure generated an anchoring friction that prevented backward slipping. The robot measured 460 mm in length, 75 mm in diameter, and demonstrated a maximum average velocity of 10 mm/s (2.17e–2 body lengths per s).

Serrano *et al.* investigated the performance improvements, in terms of forward displacement per gait cycle, that anisotropic friction in the form of printed scale-like hooks could provide a five-link snake robot measuring 48 × 48 × 475 mm.[25] To validate the impact of the scales on the inchworm and lateral undulation gaits, the robot was tested under three conditions: with scales, with the robot covered in cloth with scales, and with the robot covered in cloth without scales. Results indicated that the inclusion of scales provided a three-fold increase in the displacement per oscillation for the inchworm gait and a two-fold increase for the lateral undulation gait, when vertical actuation was incorporated.

Lee *et al.* developed micro-scale crawling robots measuring about 20 × 12 × 6 mm that utilized two linear actuators and compliant claws to perform locomotion and adhere to flat surfaces and ferromagnetic ceilings (using permanent magnets).[26] The robots successfully demonstrated locomotion and steering at a forward velocity of approximately 3.2 mm/s (0.16 body lengths per s).

Climbing machines that utilize pneumatic actuators and cylindrical, metallic brushes, with a slightly larger diameter than the pipe bore, have demonstrated an effective means of locomotion for traversing pipe and sewer systems.[27] Using a similar design concept, a miniaturized micro-machine was proposed with passive, smart bristles with curved and flat surfaces that are capable of propelling the robot through small-sized, thin pipes.[28] This concept was further investigated by Hatazaki and Ishikura *et al.*, who presented the Active Scope Camera Robot.[29,30] The robot consisted of a long cable-like structure covered with cilia in the form of thin wires oriented at a specific angle, to provide unidirectional anchorage with respect to a flat floor. It utilized a vibration and inchworm drive (pneumatic cylinder) combined with the cilia friction properties to propel the robot forward. The test robot measured 800 mm in length and 24 mm in diameter. Depending on the surface, the speed varied from 20 to 100 mm/s (0.125 body lengths per s).

Marvi *et al.* developed Scalybot,[31] a robot inspired by corn snakes, which can actively change their scales' angle of attack by contracting muscles and lifting body parts off the ground. The robot measured approximately 95 mm in length and was capable of one-dimensional rectilinear motion up to a speed of 11.7 mm/s (0.123 body lengths per s) by inclining artificially designed scales constructed from thin steel plates to actively change friction characteristics via servomotors. Other attempts to artificially replicate anisotropic friction characteristics on the micro-scale include the use of spandex, sequins and polyethylene braids,[32] inclined thin glass filaments,[33] and multi-walled carbon nanotube films oriented in mutually orthogonal directions.[34]

2.2. *Locomotion modeling*

This section overviews the literature on modeling of snake and inchworm inspired robots that utilize anisotropic friction to produce locomotion.

Hirose *et al.* formulated a mathematical description of slithering locomotion in which a snake is modeled as a continuous curve that propagates a sine wave along its length to move forward.[35] From this analysis, it was concluded that anisotropic friction was necessary to achieve snake-like locomotion using the lateral undulation gait. Hu *et al.* modeled two-dimensional slithering motion of a snake using one-dimensional curves capable of translation and heading angle rotation on a horizontal plane.[36] Theoretical analysis and experimental evaluation determined that snakes' propulsion on flat terrain relies critically on weight distribution and frictional anisotropy, which can be decomposed into three main components. The authors experimentally measured static friction coefficients of snake scales along three orthogonal directions, with results indicating that transverse μ_T, and longitudinal backwards μ_B, and forwards μ_F take on average values that satisfy the inequality $\mu_F < \mu_B < \mu_T$. By observing the dynamics of snake locomotion, the authors were able to predict a snake's forward speed during slithering motion with reasonable accuracy using mathematical models. Marvi *et al.* studied the effects of wave amplitude, frequency, and speed in snakes performing rectilinear motion, and compared their observations with a one-dimensional model of n-link crawlers. The authors used this model to compute optimal wave frequencies and amplitudes and predict the speed of a snake with 73%–97% accuracy. Results further indicated that sequentially lifting certain body segments off the ground can significantly increase the speed of rectilinear motion by up to 31%.[37] Gmiterko *et al.* modeled one-dimensional snake-like rectilinear motion using a chain of n masses with Coulomb friction anisotropy on an inclined surface. Results were used to derive the optimal number of masses to maximize forward velocity and enable a sufficient propulsive force to propel the robot up an incline.[38] Tang *et al.* developed a one-dimensional model of a three-segment snake robot, with ground interactions modeled using Coulomb dry friction. The model was used to develop the necessary conditions for both isotropic and anisotropic friction that enable the system to move from a state of rest and analyze the steady-state motion of the system; three modules were determined to be the minimum required for the isotropic friction case to achieve forward locomotion.[39] Ghanbari *et al.* investigated the planar crawling motion of an inchworm robot, modeled as a four-link robotic manipulator and simulated with Newton–Euler outward iterations.[40] Vertically lifting the majority of its front body parts off the ground generated a relatively higher frictional force which grounded the rear portion of the body and enabled the robot to extend forward.

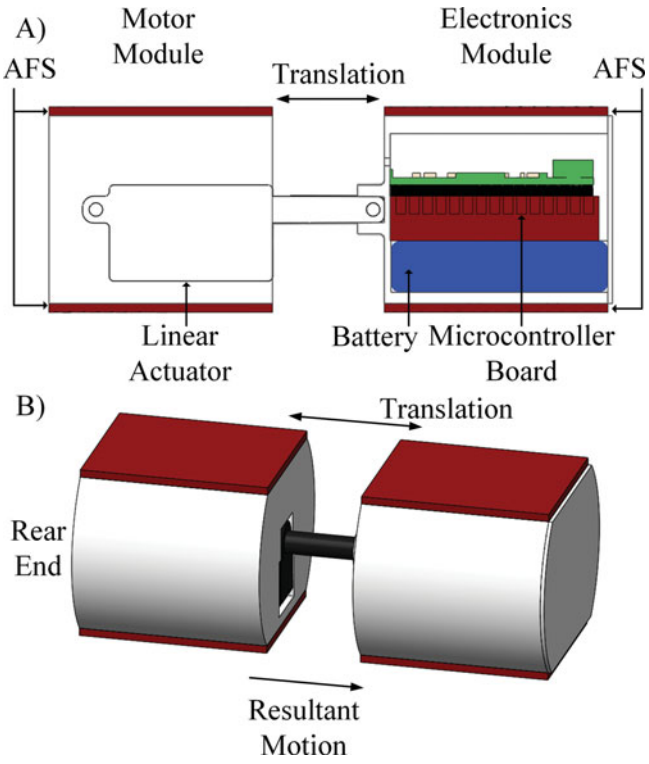

Fig. 2. (A) Cross-sectional view of the MMIR V1. (B) Assembled view depicting the forward locomotion concept.

3. Miniature Modular Inchworm Robot V1

3.1. Design concept

The concept of the MMIR was inspired by the anatomy of a biological inchworm that utilizes rectilinear expansion/contraction of its body while using anisotropic friction properties to produce locomotion. Figure 2(A) depicts a cross-sectional view of the MMIR V1. The robot consists of two main bodies—a motor module and an electronics module—which represent an inchworm's front and rear body segments and measure 44 × 44 mm in cross-section and 100 mm in length. It has a single, actuated translational DOF that is mounted within the motor module, and which provides relative translation between the two bodies, since the electronics module is rigidly connected to its shaft.

The AFS is an artificial, commercially available fabric with compliant, soft bristles, oriented at an inclination angle with respect to the robot's flat, lower surface. Therefore, the material exhibits anisotropic friction characteristics in the longitudinal (forward and backward), and transverse directions. Relative translational motion between modules will cause the robot to produce a net motion in the forward direction due to the anisotropic friction characteristics of the skin. This concept will be further investigated and demonstrated in Sections 5-7.

3.2. Electrical design

The motor module shown in Fig. 2(A) contains a micro-sized linear actuator capable of producing a 20 mm stroke length, rated for a maximum force of 35 N at a no-load speed of 25 mm/s. The actuator has an integrated resistive potentiometer, which acts as the shaft position sensor that provides displacement feedback. The electronics module contains a 450 mAh, 7.4 V battery, and an ARM Cortex M4 microcontroller that operates as the main control unit (MCU). The MCU is programmed to generate sinusoidal displacement for periodic linear expansion and contraction between the two modules.

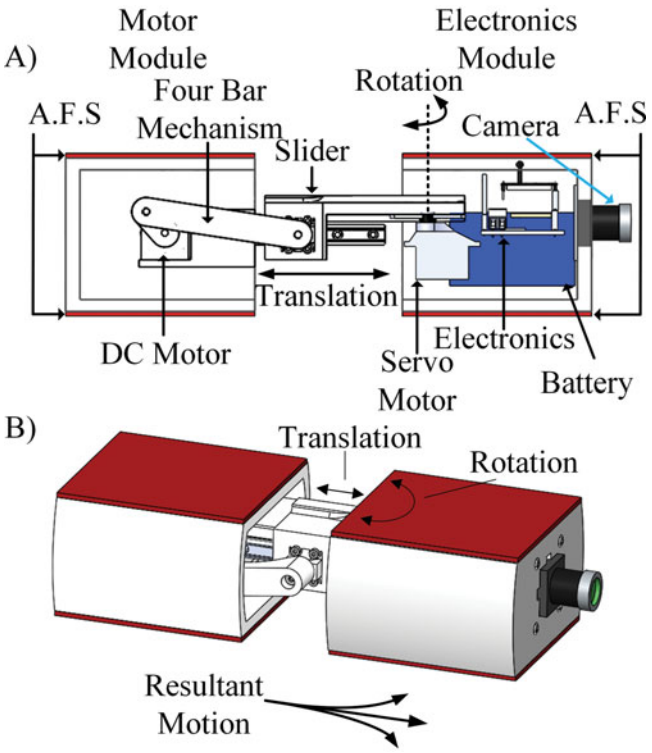

Fig. 3. (A) Cross-sectional view of the MMIR V2. (B) Assembled view depicting the planar locomotion concept.

4. Miniature Modular Inchworm Robot V2

4.1. Mechanical design

The mechanical design of the MMIR V2 is shown in a cross-sectional view depicted in Fig. 3(A). Similar to V1, the robot consists of two main bodies: a motor and electronics module. The robot measures 48 × 76 mm in cross section, and 200 mm in length. The robotic system has two-DOF since the electronics module can both translate about the sliding axis and rotate about the servo axis, relative to the motor module. The motor module houses a slider-crank four-bar mechanism that is actuated with a DC motor. Continuous rotation of the motor produces a high-frequency translational oscillation of the slider, which is connected to the horn of a servo motor. The servo motor is rigidly mounted to the electronics module.

Figure 3(B) shows an assembled view of the MMIR V2, depicting the planar locomotion concept. As in the MMIR V1, an AFS covers both the top and bottom sides of each module. Relative motion, in the form of translation and rotation between the modules, causes the robot to produce both linear and curvilinear locomotion (steering). This concept that will be further investigated in Sections 5-7.

4.2. Electrical design

The electronics module houses a 450 mAh, 7.4 V battery, which powers an ARM Cortex M4 microcontroller that operates as an MCU. The robot is teleoperated and obtains trajectory inputs from a PC-based graphic user interface over a high speed Wi-Fi network. The wireless network is powered with a high gain, 2 W antenna Wi-Fi router that enables long-range data transmission at a maximum rate of 72 Mbps.

The slider-crank four-bar mechanism is actuated with a brushed DC motor, rated for a torque of 176 N-mm at a no load speed of 450 rpm. The forward velocity of the robot is controlled by varying the crank angular velocity through the DC motor PWM command signal. The motor is controlled using the L293DD DC motor driver integrated circuit chip on the electronics module. The electronics module can be rotated with respect to the motor module via a micro RC servo motor that can provide a torque of 157 N-mm at a no load speed of 460 deg/s.

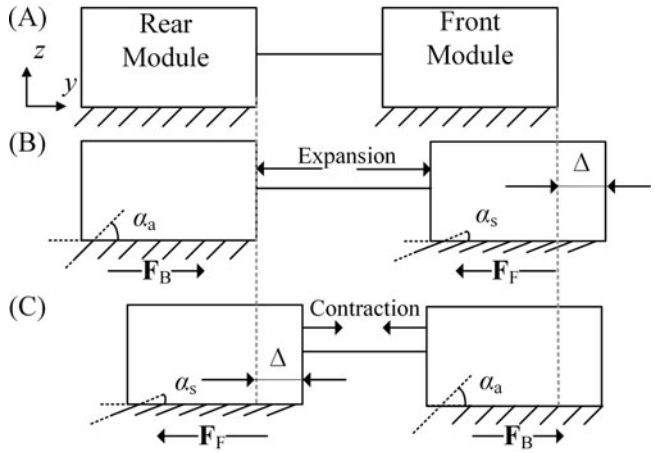

Fig. 4. Lateral view schematic diagram of the MMIR during forward locomotion: (A) start position, (B) expansion, (C) contraction.

For future applications of closed-loop trajectory tracking and mapping, the robot is equipped with a nine-axis IMU sensor to determine the orientation of each module for state estimation. The MCU uses an I^2C bus to connect to the IMU, and acquires acceleration, angular rates, and magnetic orientation at a 200 Hz update rate. The MCU has two spare UART ports, which can be used to host payload sensors, depending on application requirements. For example, the proposed prototype is equipped with a VGA camera, to acquire and wirelessly transfer still images to the user, for situational awareness and mapping applications.

5. Locomotion Strategy

This section qualitatively describes the strategy to achieve forward locomotion and steering using the robot's anisotropic friction characteristics. In this analysis, α defines the bristle inclination angle of the AFS, where the subscripts "s" and "a" represent the sliding and anchoring conditions, respectively, and where $\alpha_a > \alpha_s$.

At α_a, the bristles resemble hooks that oppose motion by anchoring themselves with micro-sized surface irregularities. Therefore, the skin exhibits a high friction coefficient μ_B in the backward direction. However, in the forward direction, the bristles can passively bend inwards to an angle α_s during sliding, to create a smoother surface which exhibits a lower friction coefficient μ_F in comparison with the anchoring configuration. It is intuitive that the transverse friction coefficient μ_T falls between high and low coefficient values $\mu_F < \mu_T < \mu_B$ (verified experimentally in Section 7). The skin's anisotropic friction characteristics, coupled with the passive, compliant nature of the material, can be used to produce locomotion.

Figure 4 shows a schematic diagram of the forward locomotion strategy of the MMIR. In this analysis, the front and rear module masses are designed to be identical (equivalent to 62.5 and 195 g for the MMIR V1 and V2, respectively), to enable efficient locomotion (minimal backward slippage).[16] Therefore, it is assumed that friction forces take on limiting values, and are dependent only on a single friction coefficient in each direction.

Figure 4(A) shows the starting configuration of the MMIR. During the expansion stroke (Fig. 4(B)), the modules move away from each other due to an actuator force. The rear module experiences a high friction force $\mathbf{F}_B$ due to a high friction coefficient μ_B, since the bristle inclination angle increases to α_a, while the front module's bristles deflect inwards to α_s. The front module thus experiences a low friction force $\mathbf{F}_F$ due to a low friction coefficient μ_F and slides forward with a displacement Δ. During the contraction stroke (Fig. 4(C)), the modules move toward each other. The front module's bristles change to α_a and resist motion with a high friction force, while the rear module's bristles flatten to α_s. During contraction, the rear module slides forward by Δ, while the front module remains stationary. Repeated iteration of steps (B)–(C) results in the forward locomotion of the robot by approximately Δ each cycle.

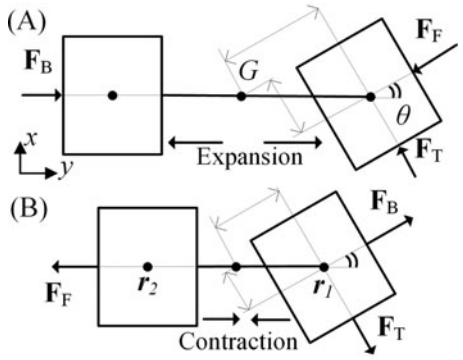

Fig. 5. Top view schematic diagram of the MMIR steering procedure: (A) expansion, (B) contraction.

Figure 5 depicts the schematic diagram of the MMIR steering procedure. In this analysis, the system's combined center of mass (CM) G, shown in Fig. 5(A), is located along the center of the line connecting each individual module's CM. The individual module CMs, assumed to be located at the center of each module, are illustrated as black dots in the figure. Relative rotation of the front module with respect to the rear module is denoted by θ.

Similar to the discussion of friction force directions during forward locomotion, Fig. 5 shows the friction force directions acting on the robot during the steering procedure. During the expansion stroke in Fig. 5(A), the forward friction force $\mathbf{F}_F$ acting on the front module creates a negative moment, whereas the transverse friction force $\mathbf{F}_T$ acting on the front module creates a positive moment about G that induces left turning. During this motion, backward friction force $\mathbf{F}_B$ does not contribute to a moment about G. For modules of equal mass, a positive value condition on the summation of moments about G, to ensure left turning, yields $\theta < \tan^{--1}(\mu_T/\mu_F)$. During the contraction stroke Fig. 5(B), the moment arising from $\mathbf{F}_B$ acting on the front module provides a positive moment, whereas transverse friction force $\mathbf{F}_T$ acting on the front module provides a negative moment about G. Similarly, left turning is achieved if $\theta > \tan^{--1}(\mu_T/\mu_B)$. Satisfying both conditions ensures that the robot will turn left during both the expansion and contraction strokes. A similar explanation describes the right steering of the robot. As noticed in this discussion and with reference to Fig. 5, all moments that cause steering originate due to rotation of the front module and all forces acting on it.

6. Dynamic Modeling

This section presents a multi-body dynamic approach to model the MMIR using generalized coordinates.[41] The system is modeled as two bodies of mass m_i, connected by a translational joint, and capable of planar motion in the global xy-plane and rotation about the z-axis (Fig. 5(B)).

Due to the relatively low mass of the four-bar mechanism relative to m_i, the translational joint between the modules is treated as a massless connection between the two bodies. The configuration of the system can be defined by a vector of generalized coordinates $\mathbf{q} = [\mathbf{q}_1, \mathbf{q}_2]^T$, where $\mathbf{q}_i = [\mathbf{r}_i, \phi_i]^T$ contains the global positions $\mathbf{r}_i = [x_i, y_i]^T$ and orientations ϕ_i of the two masses. The subscript i is used to index the two bodies, where $i = 1, 2$ refers to the electronics, motor modules. The local position vectors, denoted with the subscript ℓ, are defined as $\mathbf{r}_{\ell,\mathrm{i}} = \mathbf{R}_z^T(\phi_i)\mathbf{r}_i$, where $\mathbf{R}_z(\varphi)$ is the rotation matrix corresponding to a rotation about the z-axis by an angle φ, and where the local y-direction is oriented longitudinally (along the robot). Here, $\phi_2 = \phi_1 + \theta$, since the electronics module may rotate by an angle θ relative to the orientation of the motor module.

The sliding axis of the four-bar mechanism passes through the axis of rotation of the crank (Fig. 3). Defining $N = \|\boldsymbol{r}_1 - \boldsymbol{r}_2\|_2$ as the distance between the bodies, a distance constraint Φ^D can thus be defined, as a function of the crank angle ψ as

$$\begin{aligned} &\Phi^D \equiv N - K = 0, \\ &K = r\cos(\psi) + \sqrt{l^2 - r^2\sin^2(\psi)}, \end{aligned} \tag{1}$$

where K is the slider-crank displacement, r is the crank length, and l is the coupler link length. Specifying a constant motor angular velocity ω gives the crank angle as a function of time as $\psi = \omega t$, so that the slider-crank starts at maximum extension ($\psi = 0$). Additionally, we introduce a translational constraint to enforce the condition that the two bodies remain aligned along the axis of the slider crank. The combined constraint vector of the system, which fully defines the kinematics of the slider crank, may be written as $\Phi = [(\mathbf{\Phi}^t)^T \mathbf{\Phi}^D]^T = \mathbf{0}$, where $\mathbf{\Phi}^t$ is a 2×1 translational constraint vector, given in general form in ref. [41].

Friction is modeled by a piecewise Coulomb friction law,[38] enabling both static anchoring and dynamic sliding behaviors. Here, we allow for the possibility of velocity dependent frictional parameters to account for pre-sliding phenomena, friction lag, and other non-linear dynamic behaviors as described in ref. [42]. To account for the directional frictional properties of the AFS, directional static coefficients of friction are defined for the longitudinal and transverse directions of each module, respectively, as

$$c_{L,i} = \begin{cases} \mu_B & \text{if} \quad \dot{y}_{\ell,i} \leq 0 \\ \mu_F & \text{if} \quad \dot{y}_{\ell,i} > 0 \end{cases}, \qquad c_{T,i} = \mu_T, \tag{2}$$

where the μ terms are the constant, experimentally determined static coefficients. Similarly, longitudinal and transverse dynamic frictional parameters are defined for a linear fit approximation $m\dot{y}_{\ell,i} + b$, where the slopes $m = (m_B, m_F, \text{and } m_T)$ and the y-intercepts $b = (b_B, b_F, \text{and } b_T)$ are given, respectively, as

$$v_{L,i} = \begin{cases} m_B & \text{if} \quad \dot{y}_{\ell,i} \leq 0 \\ m_F & \text{if} \quad \dot{y}_{\ell,i} > 0 \end{cases}, \quad v_{T,i} = m_T, \qquad B_{L,i} \begin{cases} b_B & \text{if} \quad \dot{y}_{\ell,i} \leq 0 \\ b_F & \text{if} \quad \dot{y}_{\ell,i} > 0 \end{cases}, \quad B_{T,i} = b_T. \tag{3}$$

In Eqs. (2) and (3), the values of the frictional coefficients are measured experimentally (Section 7.1). As expected, empirical measurements demonstrate that m_B and m_F are approximately zero on dry terrain. The friction coefficients in (2) and (3) are stored in the matrices $\mathbf{\Omega}_{i,\mathrm{v}}$ and $\mathbf{\Omega}_{i,\mathrm{C}}$, where $\mathbf{\Omega}_{i,\mathrm{v}} = \mathrm{diag}(v_{L,i}, v_{T,i})$ is a diagonal matrix of the slopes of the dynamic coefficients, and $\mathbf{\Omega}_{i,\mathrm{C}} = \mathrm{diag}(k_{L,i}, k_{T,i})$ accounts for the Coulomb contributions. Here, $k_{L,i}$ and $k_{T,i}$ are defined as

$$k_{\{L,T\},i} = \begin{cases} c_{\{L,T\},i} & \text{if } \dot{\mathbf{r}}_{\ell,i} \cdot \hat{r}_{\ell,i} < \delta \\ B_{\{L,T\},i} & \text{if } \dot{\mathbf{r}}_{\ell,i} \cdot \hat{r}_{\ell,i} \geq \delta \end{cases}, \tag{4}$$

and account for the transition between static and dynamic friction, where δ is a small constant that defines the transition between the static and dynamic regimes, and was set at $\delta = 0.01$ in simulation.

With these definitions, the frictional force acting on body i is given by the piecewise function

$$\mathbf{F}_i = -\mathbf{R}_z(\phi_i) \left(m_i g \mathbf{\Omega}_{i,C} \mathbf{sgn}(\dot{\mathbf{r}}_{\ell,i}) + \mathbf{\Omega}_{i,v} \dot{\mathbf{r}}_{\ell,i} \right), \tag{5}$$

where g is the standard gravitational acceleration, $\mathbf{R}_z(\phi_i)$ is the rotation matrix defined previously, and **sgn** is a vector operator that performs the signum function on each element of $\dot{\mathbf{r}}_{\ell,i}$. The frictional forces calculated for each of the generalized coordinates are arranged into a total force vector $\mathbf{Q}^A$, and the body masses and moments of inertia are stored in the block diagonal mass matrix $\mathbf{M}$. Introducing a vector λ of three Lagrange multipliers, the constrained variational equations of motion may be reformulated as a differential-algebraic equation of motion (DAE). The system is defined by the DAE given by Eq. (6), in terms of the six generalized coordinates, six generalized coordinate velocities, and λ vector, where $\mathbf{\Phi_q}$ is the Jacobian, and $\boldsymbol{\gamma}$ is a vector of acceleration independent terms. Methods for evaluating and numerically solving this equation are provided in ref. [41].

$$\begin{bmatrix} \mathbf{M} & \mathbf{\Phi}_\mathbf{q}^T \\ \mathbf{\Phi_q} & \mathbf{0} \end{bmatrix} \begin{bmatrix} \ddot{\mathbf{q}} \\ \lambda \end{bmatrix} = \begin{bmatrix} \mathbf{Q}^A \\ \gamma \end{bmatrix}. \tag{6}$$

7. Results

This section presents experiments to determine the friction properties of the AFS (Section 7.1) and locomotion capabilities (Section 7.2) of the MMIR V1 and V2, which are then compared to simulated results. The performances of the MMIR robots are then compared with robots published in the literature (Section 7.3).

7.1. Experimental friction analysis

Anisotropic friction is the driving force that produces locomotion for the MMIR. The AFS provides low and high friction in the forward and backward longitudinal directions, and an intermediate friction in the transverse direction. Since friction characteristics are dependent on the nature of contact between surfaces, it is necessary to experimentally measure the friction properties of the AFS on common surface types.

The friction coefficients μ_B, μ_F, and μ_T were experimentally determined using the tilted plane method for static friction coefficients and by pulling a block mass covered with the AFS at various constant velocities for dynamic friction parameters, as described in ref. [43]. For each surface type, these trials were repeated 10 times, to compute the mean and standard deviation, $\bar{\mu} \pm \sigma$, of the static and dynamic friction parameters.

Table I presents the data of measured static and dynamic friction parameters on various surface types. It can be observed that static friction coefficient values show correlation with surface roughness. For example, the smoothest surface, anodized aluminum, shows the least significant changes in coefficient magnitude in the three directions. Carpet and concrete brick, the roughest surfaces, show the largest variation in the backward and forward (longitudinal) directions. The dynamic friction parameters (the slopes and y-intercepts) were computed using a linear fit to the experimental measurements at various constant pulling velocities. The small values of m_F, m_T, and m_B, on the order of 10^{-3} (Ns/mm), indicate the low dependence of the frictional force with respect to velocity and can be assumed to be velocity independent for future applications. For all surface types, the coefficient magnitudes obey the condition $\mu_F < \mu_T < \mu_B$. It is interesting to note that although this AFS is an artificial material, its measured static friction coefficients exhibit a similar trend as those produced by snake scales,[36] as discussed in Section 2.2.

7.2. Locomotion experiment

To assess the performance of the MMIR V1 and V2 and validate the dynamic model simulation results, two experiments were conducted with the integrated prototypes shown in Fig. 1. In the first experiment (Section 7.2.1), the robots were tracked using a vision system to compare results with simulated trajectories and study the effectiveness of producing forward and steering locomotion. In the second experiment (Section 7.2.2), the average forward velocities of the robots were measured on various surface types and compared to simulation results.

7.2.1. Locomotion tracking. In the first experiment, an optical tracking system with mm-level accuracy developed by the authors[44] was used to track the trajectories of the prototypes during rectilinear motion (Section 7.2.1.1) and steering (Section 7.2.1.2). An active marker was attached to both the electronics and motor modules of each robot to measure their positions and velocities at a high sampling rate (>200 Hz), in a 300 × 450 mm window. Experimental results were then compared to simulated results using the dynamic model derived in Section 6. Simulation results were produced using the MATLAB ode15s differential equation solver to solve Eq. (6) and simulate locomotion for MMIR V1 and V2. The electronics module CM starts from the origin, with the translational joint aligned with the global y-axis, so that the initial position is given by $\mathbf{q}_1 = [0\ l{+}r\ 0]^T$, $\mathbf{q}_2 = 0$ and $\mathrm{d}\mathbf{q}_1/\mathrm{dt} = \mathrm{d}\mathbf{q}_2/\mathrm{dt} = 0$. Mass properties and dimensions of the system were estimated using both a CAD model and physical measurements, while coefficients of friction were obtained from experimental measurements described in Section 7.1.

7.2.1.1. Rectilinear motion. For both the MMIR V1 and V2, the linear position and velocity of each module were tracked and simulated, to validate the dynamic model presented in Section 6. Rectilinear motion in the MMIR V1 was simulated by setting $\theta = 0^\circ$ and modifying the four-bar mechanism's dimensions to match the linear actuator stroke length and rotation frequency specifications given in Section 3. Figure 6 shows experimental and simulation results of MMIR V1 displacement and velocity for the two modules, oscillating with a 24 mm stroke length at 1 Hz on carpet, where y_1

Table I. Measured static friction coefficients and dynamic parameters of various surface types.

	Static			Dynamic					
Surface	μ_F	μ_T	μ_B	$m_F \times 10^{-3}$ (Ns/mm)	b_F	$m_T \times 10^{-3}$ (Ns/mm)	b_T	$m_B \times 10^{-3}$ (Ns/mm)	b_B
Anodized alum.	0.43 ± 0.02	0.44 ± 0.01	0.44 ± 0.01	1.4 ± 0.8	0.04 ± 0.8	5.3 ± 0.8	0.06 ± 0.03	6.6 ± 0.9	0.09 ± 0.03
Floor tiles (Vinyl)	0.44 ± 0.02	0.51 ± 0.02	0.57 ± 0.02	0.8 ± 1.0	0.34 ± 0.03	0.0 ± 1.0	0.50 ± 0.03	0.2 ± 1.0	0.54 ± 0.04
Polished wood	0.44 ± 0.02	0.47 ± 0.02	0.68 ± 0.04	1.2 ± 1.1	0.32 ± 0.04	1.2 ± 1.0	0.46 ± 0.05	1.9 ± 1.8	0.46 ± 0.06
Carpet	0.51 ± 0.02	0.97 ± 0.04	1.46 ± 0.08	4.3 ± 0.1	0.17 ± 0.04	0.70 ± 1.1	0.58 ± 0.06	0.6 ± 1.4	0.67 ± 0.05
Composite wood	0.43 ± 0.01	0.99 ± 0.03	1.42 ± 0.12	0.9 ± 0.9	0.33 ± 0.03	0.61 ± 0.9	0.61 ± 0.04	1.5 ± 1.0	0.77 ± 0.08
Concrete brick	0.67 ± 0.03	1.13 ± 0.11	1.52 ± 0.12	0.7 ± 1.0	0.42 ± 0.04	1.30 ± 1.0	0.46 ± 0.05	0.7 ± 1.6	0.93 ± 0.07

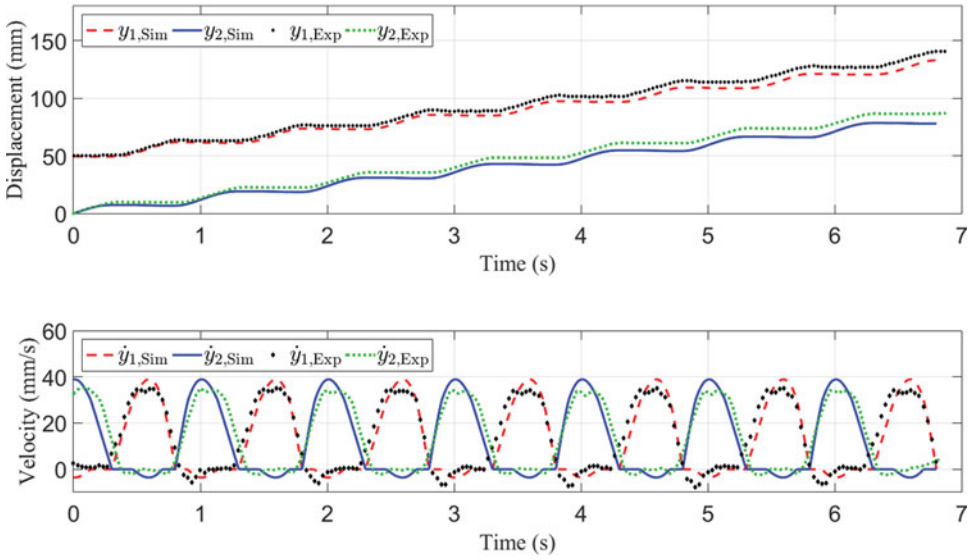

Fig. 6. MMIR V1 simulation (Sim) and experimental (Exp) at 1 Hz oscillation results of (Top) displacement and (Bottom) velocity of the two modules on carpet.

and y_2 represent the electronics and motor module positions, respectively. The step-like behavior in the displacement plot is characteristic of the robots during rectilinear motion, as described in Section 5. As one module moves forward, the other remains stationary, and the process is repeated due to oscillatory rectilinear motion. On average simulated results lagged behind experimentally measured results, corresponding to a positional tracking error of -12.3 ± 4.9 mm. The average forward velocity of the robot in simulation is approximately 12.7 mm/s. This value is somewhat less than half of the average velocity in Fig. 6, since each body motion comprises half of the robot's locomotion cycle. The velocity curves of each body have asymmetrical slopes in their acceleration and deceleration phases, due to the non-linear behavior of the slider crank. By observing the plot of the experimental velocities of the modules $\dot{y}_{1,Exp}$ and $\dot{y}_{2,Exp}$, it is interesting to note that both modules slip backward slightly and attain a small negative velocity at all instances of the stationary phase. However, the forward speed of the motor module, given by $\dot{y}_{2,Exp}$, exhibits a smaller degree of slippage at all starting instances of its stationary phase. This result indicates that the weight distribution in the assembled prototype is uneven. Although the modules were designed to match in weight, the coupling between the two modules leads to an unequal weight distribution. Variable weight distribution causes inefficient forward locomotion, with slippage as described in ref. [16] a result which falls in line with conclusions reported in ref. [36]. The modules can be observed to sharply transition between non-slipping and slipping phases due to a friction model that depends on both static and dynamic frictional parameters. The relative amplitudes of the velocities during locomotion and slipping depend on the ratios of the friction coefficients, while the transition from non-slipping to slipping depends on both friction coefficients and module mass. On average, simulated results lead experimentally measured results, corresponding to a velocity tracking error of 2.8 ± 6.0 mm/s. The experimentally observed difference in the velocity amplitudes during slipping between the two modules was reproduced in simulation by accounting for the unequal distribution of mass in the two modules, with approximately 45% of the mass in the front module and 55% in the back that resulted after assembly of the actual robotic system.

Straight-line locomotion was simulated in the same manner for the MMIR V2, the results of which are shown in Figs. 7 and 8, for low and high-frequency inchworm motion (2 Hz and 6 Hz), respectively, along with the corresponding experimental results. As in the V1 experiments, the V2 robot was run on carpet, but exhibited much higher average velocities at both oscillation frequencies. Simulated results again show close agreement with experiment after properly distributing the robot's mass between its two modules. In Fig. 7, both simulation and experimental results shift slightly out of phase but then return to being in-sync by the end of the two second time frame, which can be explained by the variability of the experimental surface conditions. By observing the velocity plots in Figs. 7 and 8, the peak magnitude of the module velocities during the slipping phase as a percent of their peak

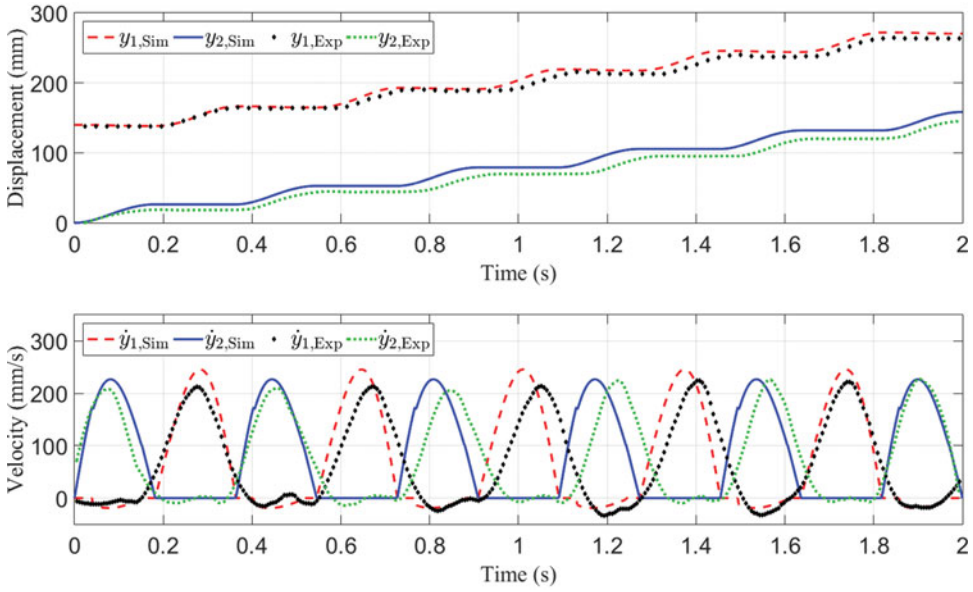

Fig. 7. MMIR V2 straight-line locomotion at low frequency (∼2 Hz). Simulation (Sim) and experiments (Exp) results are given for: (Top) displacement and (Bottom) velocity of the two modules on carpet.

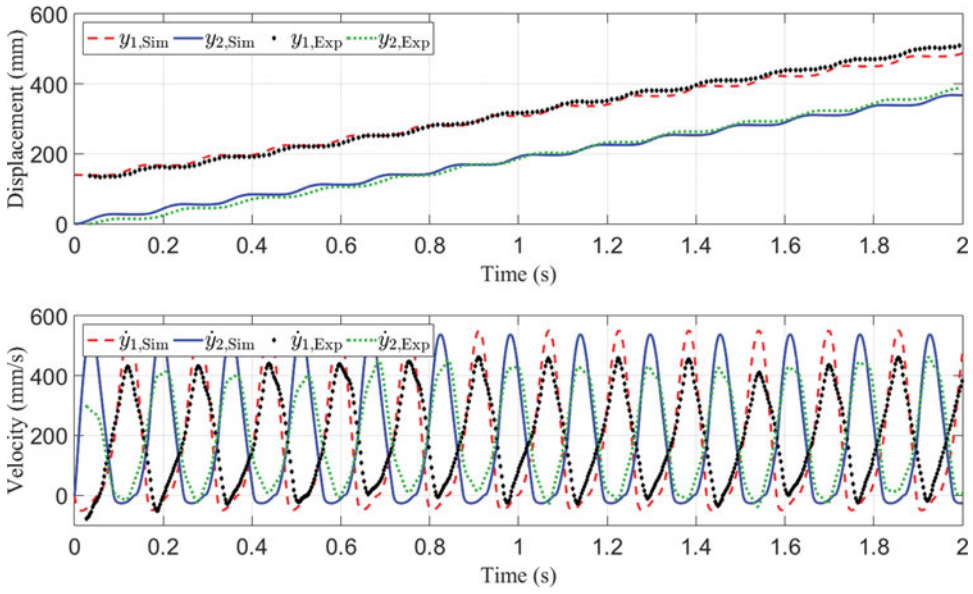

Fig. 8. MMIR V2 straight-line locomotion at high frequency (∼6 Hz). Simulation (Sim) and experiments (Exp) results are given for: (Top) displacement and (Bottom) velocity of the two modules on carpet.

magnitude during the propulsive phase was, for the electronics ($i = 1$) and motor ($i = 2$) modules, 7.77% and 0.04% for low-frequency oscillations and 9.4% and 5.0% for high frequency. This result is expected since high-frequency oscilations cause the modules to reach a peak linear velocity of up to 470 mm/s as opposed to 210 mm/s at low frequency, resulting in a larger degree of slippage. For low frequency (Fig. 7), the postion and velocity tracking errors were computing to be 13.2 ± 4.4 mm and -2.6 ± 28.0 mm/s. For high frequency (Fig. 8), the postion and velocity tracking errors were computing to be 3.8 ± 19.8 mm and -42.2 ± 73.1 mm/s.

7.2.1.2. Steering. Equation (6) was solved to simulate locomotion for MMIR V2, with the modules at various non-zero relative angle, to demonstrate forward locomotion and steering capabilities. Figure 9 presents MMIR V2 simulated and experimental results of planar locomotion trajectory

Table II. Simulated and experimentally measured average forward velocity of the MMIR V1 and V2 on various surfaces.

	Velocity (mm/s)			
	Simulated		Experimental	
Material	MMIR V1	MMIR V2	MMIR V1	MMIR V2
Anodized alum.	0	0	0	0
Floor tiles	7.5	38.7	10.3	41.2
Polished wood	9.2	69.5	11.1	86.9
Composite wood	11.1	123.1	11.7	106.5
Concrete brick	10.3	107.8	11.1	103.9
Carpet	12.5	140.1	12.7	137.9

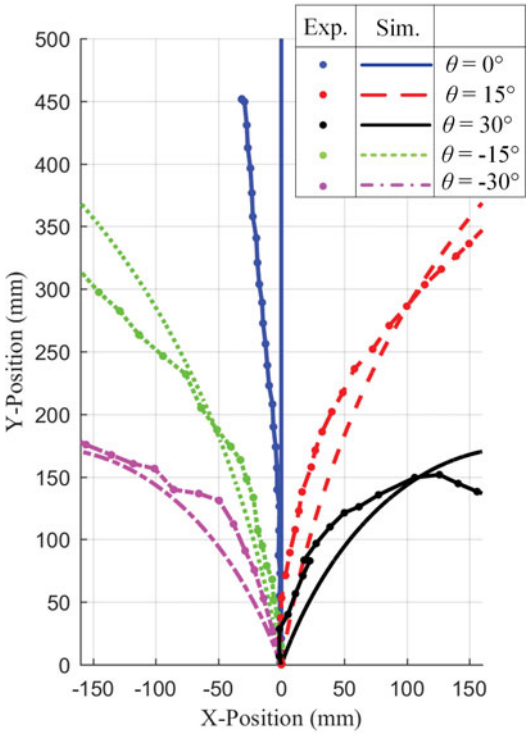

Fig. 9. MMIR V2 simulated (Sim) and experimental (Exp) results of computed trajectories of the electronics module CM during locomotion on carpet, for various values of relative angle θ.

tracking of the electronics module CM for $\theta = 0, \pm 15, \pm 30^\circ$ on carpet. The robot starts with the electronics module at the origin and a constant relative angle θ, with a slider-crank rotational frequency of 6 Hz, and stroke length of 24 mm. For each value of θ, the robot performs a turn of constant curvature. From Fig. 9 experimental results, it can be observed that the prototype (1) produces approximately straight line motion for $\theta = 0^\circ$, (2) achieves a greater curvature for larger relative angle θ, and (3) exhibits approximate symmetry for relative angles of equal but opposite magnitude.

The main factors which cause deviations between experimentally measured and idealized, computed simulation trajectories (Fig. 9), are assembly errors caused by minor rotational play in the slider-crank mechanism and slight misalignment of the servomotor rotation axis. As the servomotor rotates to create a relative angle, a slight rotational-axis misalignment can cause significant variations in the contact surface between the two modules, which results in anti-symmetric behavior. In addition, it is expected that variations in surface conditions and the collection of small debris within the bristles of the AFS can also cause locomotion deviations.

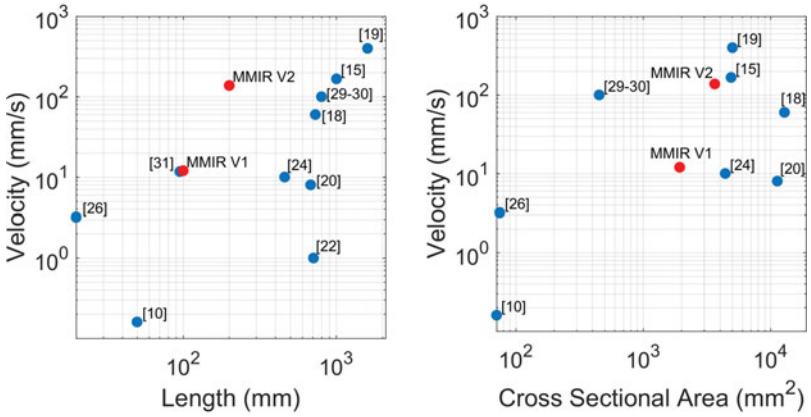

Fig. 10. (Left) Velocity-length plot, and (Right) velocity-area plot of similar robots found in literature.

7.2.2. Maximum forward velocity. The maximum forward velocities of the MMIR robots were measured on various surface types. For each surface, experiments were conducted 10 times to compute the average of the maximum forward velocity. Table II shows the measured average forward velocities of MMIR V1 and V2 in comparison to the simulated maximum velocities estimated using the dynamic model derived in Section 6. The prototypes failed to produce any forward motion on anodized aluminum, due to the forward and backward coefficients of friction being the same (Table I). On the remaining surfaces, the robots successfully moved forward with various velocities due to the anisotropic friction coefficients. The MMIR V1 and V2, at maximum oscillating frequency, 1 Hz and 6 Hz respectively, were able to achieve a maximum forward velocity of 12.7 mm/s and 137.9 mm/s, respectively. MMIR V2 demonstrates a faster velocity, due to the slider-crank four-bar mechanism, which can produce faster relative translation in comparison to the linear actuator used in V1. With reference to Table II, it can be seen that the dynamic model presented in Section 6 predicts the robotic system's forward velocity with an accuracy of 73%–98.5%, similar to the 73%–97% accuracy of the model reported in ref. [37].

7.3. Comparitive analysis

To compare the performance of the MMIR V1 and V2 with the robots reviewed in Section 2, Fig. 10 illustrates velocity-length and velocity-area (cross-sectional) plots and Table III presents the body length per second performance criterion. With reference to Fig. 10, it is interesting to note that both the MMIR V1 and V2 produce a relatively higher forward velocity for robots of similar length dimensions. The MMIR V2 is capable of producing a significantly higher forward velocity than existing robots of length <800 mm and cross-sectional area <4400 mm^2. Of the robots in Table III, the MMIR V2 demonstrates the highest ratio of body lengths per second, surpassing the active cord mechanism robot[19] by 175%, which utilized a slithering gait of propagated sine waves and ratchet wheels covering its body for forward locomotion on flat terrain. These results indicate that the four-bar slider-crank mechanism coupled with the proposed AFS can provide a millimeter scale robot an effective means of producing high-speed locomotion while maintaining a small length and cross-section, with respect to the various robots proposed in the literature.

8. Conclusion and Future Work

This paper presents the design evolution of an inchworm robot that utilizes undulatory rectilinear-gait motion of modules covered with AFS to produce locomotion. The use of AFS results in a simple, low-cost, miniature mechanical structure. The MMIR V1 is capable of producing one-dimensional forward locomotion with a maximum forward velocity of 12.7 mm/s. The MMIR V2 utilizes a slider-crank four-bar mechanism and servomotor to produce high-frequency relative translation and rotation, to increase forward velocity and enable turning capabilities. It demonstrated a maximum forward velocity of 137.9 mm/s. The MMIR V2 exhibits a maximum speed of 0.689 body lengths per

Table III. Body lengths per second criteria of similar robots found in the literature.

Robot	Body lengths per second (s^{-1})
MMIR V2	0.689
Active cord mechanism–R5 robot[19]	0.25
Maryland snake inspired robot[15]	0.167
Inchworm robots with bidirectional passive claws[26]	0.160
MMIR V1	0.127
Active scope camera robot[29,30]	0.125
Scalybot[31]	0.123
Slim slime robot[18]	8.21e–2
Earthworm-like robot with shape memory alloy actuator[24]	2.17e–2
Snake robot with unidirectional wheels[20]	1.17e–2
Earthworm-like micro robot with a shape memory alloy actuator[10]	3.20e–3
Planar walker[23]	1.41e–3

second, which surpasses the performance of existing robots that utilize anisotropic friction to produce locomotion by up to 175%.

Locomotion-tracking experimental results demonstrated qualitative and quantitative agreement with simulated position and velocity profiles of the dynamic model. However, deviations from the idealized locomotion trajectories were observed to be caused by slippage, assembly errors, and variations in surface conditions and weight distribution. The dynamic model presented in this work predicts the robotic system's forward velocity with an accuracy of 73%–98.5%, similar to the 73%–97% accuracy of the model reported in ref. [37]. As the MMIR relies on anisotropic friction to produce locomotion, backward slippage occurs if the actuator force exceeds the static friction force. This characteristic was captured using the developed dynamic model and was corroborated experimentally. Based on the results of this work, and[37] improving the lower bound accuracy of the dynamic model to match experimental performance is a challenging task due to surface condition variations and debris collection that vary friction characteristics (as discussed in Section 7.2.1). Future research into the utilization of slip detection sensors and AFS materials that do not collect debris during operation merit investigation to improve the accuracy of dynamic models and physical performance of robots that rely on anisotropic friction to produce locomotion. The authors will further investigate methods to utilize acceleration measurements from the IMU to detect backward slippage and control actuator force. By minimizing slippage, the power efficiency of the robot can be improved for longer operation time. Furthermore, magnetometer and gyroscope measurements will be used to implement an attitude heading and reference system for closed-loop steering control. These factors will be accounted for as part of future work to better replicate experimental results.

The robotic system is currently limited to locomotion on flat surfaces due to its rigid structured mechanical design and construction. However, since the AFS is a soft, compliant material it may be placed on deformable soft bodies to enable the robotic system to produce locomotion on rugged terrain. Furthermore, the incorporation of an AFS on compliant bodies may also enable the robot to squeeze through conduits that measure smaller than its undeformed body cross-sectional area; thus, enabling performance similar to biological inchworm specimens.

References

1. K. Autumn and A. M. Peattie, "Mechanisms of adhesion in geckos," *Integrative Comparative Biol.* **42**, 1081–1090 (2002).
2. M. W. Denny, "A quantitative model for the adhesive locomotion of the terrestrial slug, Ariolimax columbianus," *J. Exp. Biol.* **91**, 195–217 (1981).
3. N. Stork, "Experimental analysis of adhesion of Chrysolina polita (Chrysomelidae: Coleoptera) on a variety of surfaces," *J. Exp. Biol.* **88**, 91–108 (1980).
4. M. Spenko, G. C. Haynes, J. A. Sanders, M. R. Cutkosky, A. A. Rizzi, R. J. Full and D. E. Koditschek, "Biologically inspired climbing with a hexapedal robot," *Departmental Papers (ESE)* 397 (2008).
5. S. Kim, A. T. Asbeck, M. R. Cutkosky and W. R. Provancher, "SpinybotII: Climbing Hard Walls with Compliant Microspines," *Proceedings of the* 12th International Conference on Advanced Robotics, Seattle, WA, USA (2005) pp. 601–606.

6. S. Kim, M. Spenko, S. Trujillo, B. Heyneman, V. Mattoli and M. R. Cutkosky, "Whole Body Adhesion: Hierarchical, Directional and Distributed Control of Adhesive Forces for a Climbing Robot," *Proceedings of the International Conference on Robotics and Automation*, Roma, Italy (2007) pp. 1268–1273.
7. P. Birkmeyer, K. Peterson and R. S. Fearing, "DASH: A Dynamic 16g Hexapedal Robot," *Proceedings of the International Conference on Intelligent Robots and Systems*, St. Louis, MO, USA (2009) pp. 2683–2689.
8. S. Kim, J. E. Clark and M. R. Cutkosky, "iSprawl: Design and tuning for high-speed autonomous open-loop running," *Int. J. Robot. Res.* **25**, 903–912 (2006).
9. U. Saranli, M. Buehler and D. E. Koditschek, "RHex: A simple and highly mobile hexapod robot," *Int. J. Robot. Res.* **20**, 616–631 (2001).
10. B. Kim, M. G. Lee, Y. P. Lee, Y. Kim and G. Lee, "An earthworm-like micro robot using shape memory alloy actuator," *Sensors Actuators A: Phys.* 125, 429–437 (2006).
11. J.-S. Koh and K.-J. Cho, "Omegabot: Biomimetic Inchworm Robot using sma Coil Actuator and Smart Composite Microstructures (scm)," *Proceedings of the International Conference on Robotics and Biomimetics*, Guilin, China (2009) pp. 1154–1159.
12. J. Lim, H. Park, J. An, Y.-S. Hong, B. Kim and B.-J. Yi, "One pneumatic line based inchworm-like micro robot for half-inch pipe inspection," *Mechatronics* 18, 315–322 (2008).
13. J. K. Hopkins, B. W. Spranklin and S. K. Gupta, "A survey of snake-inspired robot designs," *Bioinspiration Biomimetics* **4**, 021001 (2009).
14. G. S. Chirikjian and J. W. Burdick, "The kinematics of hyper-redundant robot locomotion," *IEEE Trans. Robotics Autom.* **11**, 781–793 (1995).
15. J. K. Hopkins and S. K. Gupta, "Design and modeling of a new drive system and exaggerated rectilinear-gait for a snake-inspired robot," *J. Mechanisms Robot.* **6**, 021001 (2014).
16. W. Saab and P. Ben-Tzvi, "Design and Analysis of a Miniature Modular Inchworm Robot," *Proceedings of the International Design Engineering Technical Conferences and Computers and Information in Engineering Conference*, Charlotte, NC, USA (2016).
17. M. Schulke, L. Hartmann and C. Behn, "Worm-like Locomotion Systems: Development of Drives and Selective Anisotropic Friction Structures," *Proceedings of the 56th International Scientific Colloquium*, Ilmenau, Germany (2011).
18. H. Ohno and S. Hirose, "Design of Slim Slime Robot and its Gait of Locomotion," *Proceedings of the International Conference on Intelligent Robots and Systems* (2001) pp. 707–715.
19. S. Hirose and H. Yamada, "Snake-like robots [tutorial]," *IEEE Robot. Autom. Mag.* **16**, 88–98 (2009).
20. W. Tang, F. Reyes and S. Ma, "Study on Rectilinear Locomotion based on a Snake Robot with Passive Anchor," *Proceedings of the International Conference on Intelligent Robots and Systems*, Hamburg, Germany (2015) pp. 950–955.
21. K. Wang and S. Ma, "Kinematic Analysis of Snake-Like Robot Using Sliding Joints," *Proceedings of the International Conference on Robotics and Biomimetics*, Tianjin, China (2010) pp. 1484–1489.
22. I. Chen, S. H. Yeo and Y. Gao, "Locomotive gait generation for inchworm-like robots using finite state approach," *Robotica* **19**, 535–542 (2001).
23. S. H. Y. I.-M. Chen and R. S. P. S. Wong, "Design and Development of a Planar Inchworm Robot," *Proceedings of the 17th IAARC International Symposium on Automation and Robotics in Construction*, Taipei, Taiwan (2000).
24. H. Fang, C. Wang, S. Li, K. W. Wang and J. Xu, "A comprehensive study on the locomotion characteristics of a metameric earthworm-like robot," *Multibody Syst. Dynamics* **35**, 153–177 (2015).
25. M. M. Serrano, A. H. Chang, G. Zhang and P. A. Vela, "Incorporating Frictional Anisotropy in the Design of a Robotic Snake Through the Exploitation of Scales," *Proceedings of the International Conference on Robotics and Automation*, Seattle, Washington, USA (2015) pp. 3729–3734.
26. D. Lee, S. Kim, Y.-L. Park and R. J. Wood, "Design of Centimeter-Scale Inchworm Robots with Bidirectional Claws," *Proceedings of the International Conference on Robotics and Automation*, Shanghai, China (2011) pp. 3197–3204.
27. E. Appleton and N. W. Stutchbury, "Novel brush drive robotic tractor for sewer and water main inspection and maintenance," *Ind. Robot: An Int. J.* **27**, 370–377 (2000).
28. M. Dovica, M. Gorzás, J. Kováč and Š. Ondočko, "In-pipe Passive Smart Bristled Micromachine," *Proceedings of the 2nd Slovakian-Hungarian Joint Symposium on Applied Machine Intelligence*. Retrieved from http://www.bmf.hu/conferences/SAMI2004/dovica.pdf (2004).
29. K. Hatazaki, M. Konyo, K. Isaki, S. Tadokoro and F. Takemura, "Active Scope Camera for Urban Search and Rescue," *Proceedings of the International Conference on Intelligent Robots and Systems*, San Diego, CA, USA (2007) pp. 2596–2602.
30. M. Ishikura, K. Wakana, E. Takeuchi, M. Konyo and S. Tadokoro, "Running Performance Evaluation of Inchworm Drive and Vibration Drive for Active Scope Camera," *Proceedings of the International Conference on Advanced Intelligent Mechatronics*, Budapest, Hungary (2011) pp. 599–604.
31. H. Marvi, G. Meyers, G. Russell and D. L. Hu, "Scalybot: A Snake-Inspired Robot with Active Control of Friction," *Proceedings of the Dynamic Systems and Control Conference*, Arlington, Va (2011) pp. 443–450.
32. K. J. Dowling, Limbless Locomotion: Learning to Crawl with a Snake Robot *Ph.D. Thesis* (Pittsburgh, PA: The Robotics Institute, Carnegie Mellon University, 1996).
33. M. Schulke, Entwurf, Steuerung und Analyse Biomimetischer, Wurmartiger Bewegungssysteme *Masters Thesis* (Ilmenau, Germany: Diplomarbeit, TU Ilmenau, Fakultät für Maschinenbau, 2011).

34. P. Dickrell, S. Sinnott, D. Hahn, N. Raravikar, L. Schadler, P. Ajayan and G. Sawyer, "Frictional anisotropy of oriented carbon nanotube surfaces," *Tribology Lett.* 18, 59–62 (2005).
35. S. Hirose and M. Mori, "Biologically Inspired Snake-like Robots," *Proceedings of the International Conference on Robotics and Biomimetics*, Shenyang, China (2004) pp. 1–7.
36. D. L. Hu, J. Nirody, T. Scott and M. J. Shelley, "The mechanics of slithering locomotion," *Proc. Nat. Acad. Sci.* **106**, 10081–10085 (2009).
37. H. Marvi, J. Bridges and D. L. Hu, "Snakes mimic earthworms: Propulsion using rectilinear travelling waves," *J. Royal Soc. Interface* **10**, 20130188 (2013).
38. A. Gmiterko, M. Kelemen and I. Virgala, "The snake rectilinear motion modeling on the flat inclined surface," *Int. J. Mech. Appl.* **2**, 39–42 (2012).
39. W. Tang and S. Ma, "Analysis of Rectilinear Motion of a Three-Segment Snake Robot Under Action of Dry Friction," *Proceedings of the International Conference on Robotics and Automation*, Seattle, Wa (2015) pp. 3723–3728.
40. A. Ghanbari, A. Rostami, S. M. R. S. Noorani and M. M. S. Fakhrabadi, *Modeling and Simulation of Inchworm Mode Locomotion*, vol. 5314 (Springer, Berlin, Heidelberg, 2008).
41. E. J. Haug, *Computer Aided Kinematics and Dynamics of Mechanical Systems*, vol. 1 (Allyn and Bacon Boston, Boston, Ma, 1989).
42. B. Tijani Ismaila, M. Salami, R. Akmeliawati and H. Alfaro, "Artificial Intelligent Based Friction Modelling and Compensation in Motion Control System," **In:** *Advances in Mechatronics* (InTech, Shanghai, China, 2011).
43. A. Harnoy, B. Friedland and S. Cohn, "Modeling and measuring friction effects," *IEEE Control Syst.* **28**(6) (2008).
44. A. Kumar and P. Ben-Tzvi, "Spatial object tracking system based on Linear Optical Sensor Arrays (LOSA)," *IEEE Sensors J.* **16**(22), 7933–7940 (2016).